AGU PUBLICATIONS

Geophysical Research Letters

RESEARCH LETTER
10.1002/2016GL071310

Key Points:
- Optimal time alignment (OTA) overcomes known modeling issues of tsunami tide-gauge records for source inversion
- Synthetic tests are used to illustrate and validate the new method showing how OTA significantly improves the retrieved source model
- With OTA method the tsunami source of the Illapel earthquake is displaced trenchward

Supporting Information:
- Supporting Information S1
- Table S1
- Table S2

Correspondence to:
F. Romano,
fabrizio.romano@ingv.it

Citation:
Romano, F., A. Piatanesi, S. Lorito, C. Tolomei, S. Atzori, and S. Murphy (2016), Optimal time alignment of tide-gauge tsunami waveforms in nonlinear inversions: Application to the 2015 Illapel (Chile) earthquake, *Geophys. Res. Lett.*, *43*, doi:10.1002/2016GL071310.

Received 22 SEP 2016
Accepted 23 OCT 2016
Accepted article online 25 OCT 2016

Optimal time alignment of tide-gauge tsunami waveforms in nonlinear inversions: Application to the 2015 Illapel (Chile) earthquake

F. Romano[1], A. Piatanesi[1], S. Lorito[1], C. Tolomei[1], S. Atzori[1], and S. Murphy[1]

[1]Istituto Nazionale di Geofisica e Vulcanologia, Rome, Italy

Abstract Tsunami waveform inversion is often used to retrieve information about the causative seismic tsunami source. Tide gauges record tsunamis routinely; however, compared to deep-ocean sensor data, tide-gauge waveform modeling is more difficult due to coarse/inaccurate local bathymetric models resulting in a time mismatch between observed and predicted waveforms. This can affect the retrieved tsunami source model, thus limiting the use of tide-gauge data. A method for nonlinear inversion with an automatic optimal time alignment (OTA), calculated by including a time shift parameter in the cost function, is presented. The effectiveness of the method is demonstrated through a series of synthetic tests and is applied as part of a joint inversion with interferometric synthetic aperture radar data for the slip distribution of the 2015 M_w 8.3 Illapel earthquake. The results show that without OTA, the resolution on the slip model degrades significantly and that using this method for a real case strongly affects the retrieved slip pattern.

1. Introduction

Tsunami data inversions have provided very important information regarding the tsunamigenic component of the earthquake source process since their first application [e.g., *Satake*, 1987] through the last two decades that have been characterized by a large number of great earthquakes and tsunamis [*Lay*, 2015; *Lorito et al*., 2016].

Tsunami source studies can be performed by using tsunami data only [e.g., *Satake*, 1987; *Piatanesi and Lorito*, 2007], or jointly with other kinds of geophysical data [e.g., *Lorito et al*., 2011], which allows for the exploitation of complementary information regarding the causative source.

Tide gauges have been used as primary source of sea level information since the midnineteenth century (http://noc.ac.uk/science-technology/climate-sea-level/sea-level/tides/tide-gauges/tide-gauge-instrumentation); however, they were designed for recording longer-term variations than tsunamis, and their locations are generally not ideal for tsunami source studies, since they are in very shallow waters or semiclosed basins and harbors.

Nevertheless, tsunami waveforms recorded by tide gauges carry valuable information on the tsunami source. When using these signals for source inversion studies, the most common practice is to consider only their first cycles, which are less affected by the complexity and nonlinearity of local wave propagation around the instrument [e.g., *Fujii and Satake*, 2006].

Even so, a time mismatch is often found between the observed and modeled tsunami waveforms, with the latter arriving generally earlier [e.g., *Heidarzadeh et al*., 2016]. These early arrivals of the synthetic waveforms are mainly due to an inaccurate or too coarse bathymetric model, or to unknown or unaccounted for instrumental response, and possible unknown clock error of old instruments. In order to model these effects properly, a high-resolution bathymetric grid around the instrument location would be necessary, but such data are not always publicly available; moreover, a lower spatial resolution for tsunami modeling reduces the associated computational cost.

Clearly, this time mismatch may affect the tsunami source model inferred by data inversion, e.g., the earthquake slip distribution. This limitation in using tide-gauge data in inversion problems is typically circumvented by trying to manually (and subjectively) aligning the waveforms, sometimes with a trial and error approach [e.g., *Fujii and Satake*, 2006; *Lorito et al*., 2011].

Other types of instruments, such as the DART buoys (http://www.ndbc.noaa.gov/dart.shtml), or specifically developed tsunameters, are typically placed in deep waters and do not suffer from this issue. In some cases,

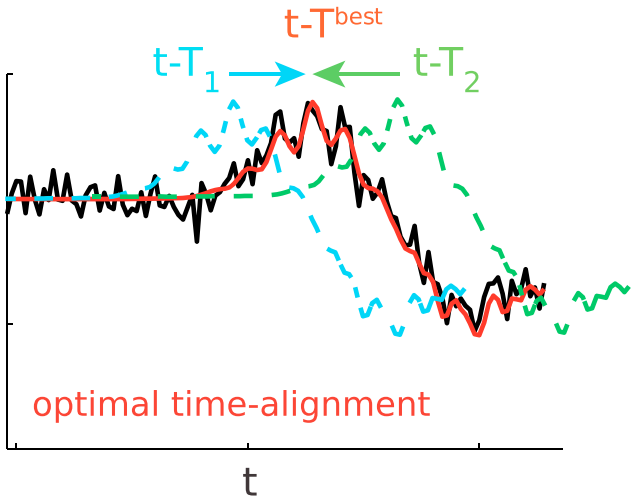

Figure 1. Cartoon of the optimal time alignment. The solid black line represents a noisy observed tsunami waveform; the green and cyan dashed lines represent the predicted tsunami waveforms shifted in time; T_1 and T_2 indicate two discrete time shift possibly explored during the inversion; the solid red line represents the predicted tsunami waveform shifted in time by T_{best} (the time shift that minimizes the cost function).

for example, the 2011 Tohoku tsunami, they have provided an unprecedented amount of information about the tsunami source [e.g., *Simons et al.*, 2011; *Bletery et al.*, 2014; *Romano et al.*, 2014]. Nevertheless, their azimuthal coverage around the tsunami source is not always optimal; therefore, the addition of tide-gauge data would be desirable.

In this study we propose a simple method for optimal time alignment between observed and synthetic data, partially borrowed from seismology, that to our best knowledge has never been used in tsunami inversions. It is based on minimizing the misfit of the waveforms within a nonlinear inversion scheme, where a time shift at each station is included as free parameter along with the source features in the cost function. The source model is thus retrieved simultaneously with the station time shifts.

We illustrate the method and show its effectiveness by means of a series of synthetic tests; then we apply the method to a real case, the 16 September 2015 great megathrust earthquake (M_w 8.3) which occurred ~47 km W offshore Illapel, Chile, where differences in arrival times between observed and predicted tsunami waveforms have been found [e.g., *Heidarzadeh et al.*, 2016].

2. The Optimal Time Alignment Method and Its Application to a Synthetic Case

We propose an approach to the tsunami data inversion that takes into account possible time shifts between observed and predicted tsunami signals. In seismological studies [e.g., *VanDecar and Crosson*, 1990; *Mercerat and Nolet*, 2013; *Kimman*, 2016; *Yuan et al.*, 2016] time shift issues of seismic waveforms which arise for a number of different reasons (e.g., inaccuracies of the Earth seismic velocity model, simplifying assumptions about the source time function or in the wave propagation theory) are often considered and addressed in various ways. For example, in double-difference seismic tomography the time shift between observed and synthetic seismic waveforms has been mapped into the seismic velocity model by using waveform cross correlation [*Zhang and Thurber*, 2003].

In this study, a time shift is used to minimize the tsunami cost function in a nonlinear inversion, which measured the misfit between observed and predicted tsunami waveforms:

$$E(T) = 1 - \frac{2\int_{t1}^{t2} \mathrm{obs}(t)\,\mathrm{synt}(t-T)\,\mathrm{d}t}{\int_{t1}^{t2} \mathrm{obs}^2(t)\,\mathrm{d}t + \int_{t1}^{t2} \mathrm{synt}^2(t-T)\,\mathrm{d}t} \quad (1)$$

where obs and synt are the observed and synthetic waveforms, respectively; $t1$ and $t2$ delimit the time window used for inverting each data; and T is the time shift tested within the cost function E.

This assumes that rigid time shifts occur during propagation/recording and may be different at each station. Therefore, the aim is to avoid that these shifts are incorrectly mapped onto the source parameters (e.g., subfault slip and average rupture velocity). Placing the time shift directly into the cost function used in nonlinear inversion allows for finding, simultaneously with the source model, the nonsubjective automatic optimal time alignment (hereinafter OTA) that minimizes the global mismatch between synthetic and observed data for all the waveforms. The cartoon in Figure 1 illustrates the effect on each waveform.

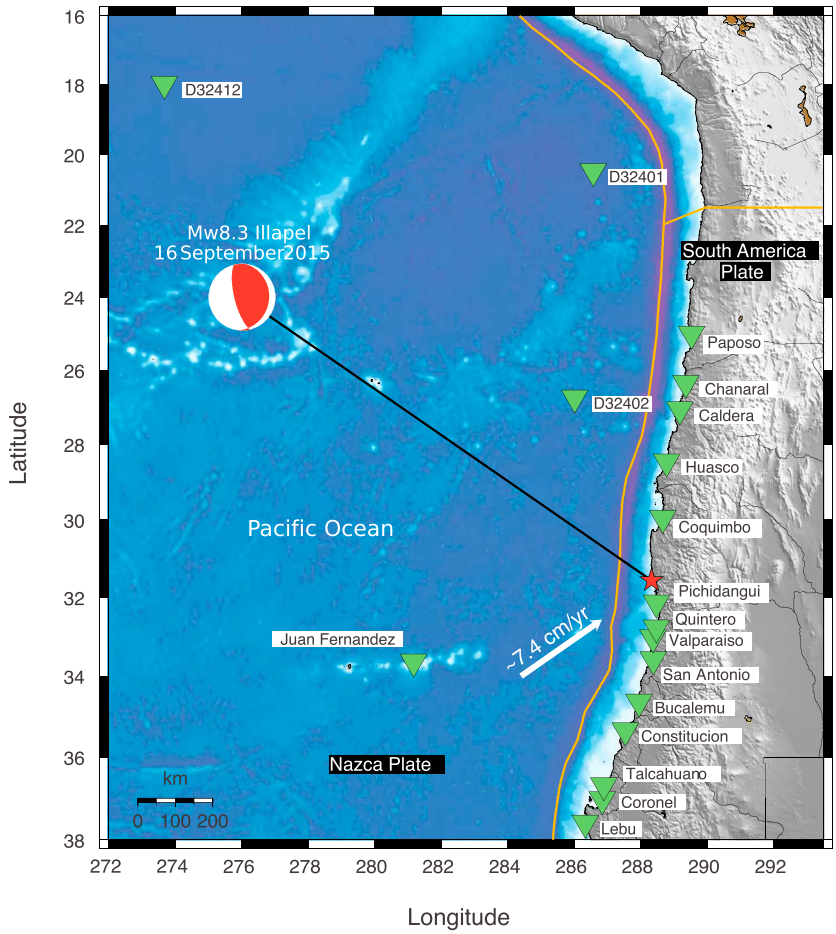

Figure 2. Location map of the 2015 Illapel earthquake. The red star and red and white "beach ball" indicate epicenter and focal mechanism of the earthquake, respectively (*Global Centroid Moment Tensor*, http://www.globalcmt.org/). The green triangles indicate the tide gauges and the DART buoys used in this study. The white arrow indicates the approximate convergence direction of the Nazca plate.

However, for complex earthquake rupture history (i.e., long/delayed rupture or low slip velocity [e.g., *Lee et al.*, 2016]) the whole waveforms would be not affected by a rigid shift but just a more complex modification of the full waveform. This is a well-known issue that the OTA method does not account for and that is beyond the scopes of the method. Indeed, whereas the OTA prevents to map the time shift due to the tsunami propagation in the slip distribution, the method per se cannot avoid to map in the slip distribution a very complex rupture history (i.e., trade-off between rupture velocity and slip distribution). This can be treated only by inverting for the kinematic rupture parameters, provided that the tsunami data can resolve them, e.g., for very long ruptures [e.g., 2004 Sumatra earthquake; *Lorito et al.*, 2016, and references therein], extremely low rupture/slip velocity as for tsunami earthquakes, and instruments in the near field [e.g., 2011 Tohoku earthquake; *Satake et al.*, 2013]. In this study, we imposed a constant rupture velocity according to seismological studies (that better constrain this parameter) and an instantaneous rise time.

We develop and test the method in the area of the 2015 Illapel M_w 8.3 earthquake [*Melgar et al.*, 2016; *Tilmann et al.*, 2016; *Lay et al.*, 2016; *Heidarzadeh et al.*, 2016], whose tsunami waves have been measured by several tide gauges and some DART buoys (Figure 2). We set up a joint inversion of tsunami and interferometric synthetic aperture radar (InSAR) data recorded on occasion of the Illapel event, in order to exploit their joint resolving power while retrieving the earthquake source [e.g., *Lorito et al.*, 2016]. This is a case study; the method is general and could be applicable to any earthquake source whose tsunami is recorded by multiple tide gauges.

2.1. Fault Parameterization and Green's Functions

The hypocenter of the Illapel event was located along the subduction interface between the Nazca and South America plates; thus, a fault model consistent with the geometry of the Nazca plate subduction interface was built by using the strike and dip variation from the Slab1.0 model [*Hayes et al*., 2012]; the fault surface was subdivided into 160 quadrilateral subfaults each with a size of ~20 × 20 km (Table S1 and Figure S1 in the supporting information).

Each quadrilateral subfault was subdivided into pairs of adjacent triangles [*Romano et al*., 2012], where the three components of the deformation at each point of the InSAR data set was computed analytically assuming a homogeneous half-space approximation [*Meade*, 2007]. Since the InSAR data used in this study are line-of-sight components of the three-dimensional deformation field, the Green's functions were obtained by combining the three components of the deformation by using appropriate coefficients.

Additionally, the horizontal and vertical displacements of the seafloor were computed for each subfault, and the horizontal displacement of the oceanic slope in the trench zone was then converted into an effective vertical displacement following *Tanioka and Satake* [1996]. Filtering of the seafloor deformation through the water column was modeled following *Kajiura* [1963]. With this initial condition, tsunami Green's functions were numerically computed with NEOWAVE [*Yamazaki et al*., 2009, 2011], a nonlinear nonhydrostatic weakly dispersive code that models the tsunami propagation. The bathymetry model used for the numerical tsunami simulation was SRTM15 (http://topex.ucsd.edu/WWW_html/srtm30_plus.html). Wet-dry moving boundary and full-wave transmission were used at the coast and at open sea, respectively. A two-level system of nested computational grids with different spatial resolution was adopted to model the tsunami propagation down to the resolution of 1 arc min at three DART buoys and 0.25 arc min at 15 tide gauges along the Chilean coast (Figure 2).

2.2. Checkerboard Test for Single and Joint Inversions of Tsunami and InSAR Data With and Without Optimal Time Alignment (OTA) of Tsunami Waveforms

Our target model was a checkerboard slip distribution with alternate slip values of 0 and 10 m on adjacent groups of 2 × 2 subfaults (Figure 3a) with rake values (85°, 100°, and 115°) fixed on three large blocks. A circular rupture front propagating from the hypocenter with rupture velocity of 2 km/s was assumed.

Synthetic tsunami and InSAR data sets were created from the checkerboard distribution and used as "observed" data in the inversions. We corrupted both data sets by adding Gaussian random noise with a variance of 10% of the clean tsunami waveforms and InSAR deformation, respectively. Moreover, we shifted in time the target synthetic tsunami waveforms (for both tide gauges and DART stations) by adding a random delay in a range of 0–15 min in order to mimic the typically observed early arrival of the predicted tsunami signals.

The inverse problem was solved by means of the heat-bath algorithm, a particular implementation of the simulated annealing [*Rothman*, 1986; *Piatanesi and Lorito*, 2007]. Two different cost functions were used for the two data sets. A cost function that was used in previous tsunami inversions [e.g., *Romano et al*., 2015], but modified by the inclusion of the time shift parameter T, was applied to the DART and tide-gauge data (equation (1)); an L2 norm was used for InSAR data.

In order to obtain a balance between the two data sets in the joint inversion, different weights for each cost function were assigned based on trial and error approach [e.g., *Lorito et al*., 2016, and references therein]: where in this case of this study a tsunami/InSAR weight ratio of 1/5 was applied.

When only the InSAR data were inverted (Figure 3b, data fit in Figure S2), as expected the pattern of slip was well reconstructed only for slip occurring not too far offshore [e.g., *Romano et al*., 2010; *Lorito et al*., 2011]. When inverting tsunami data only without applying the OTA, i.e., fixing $T = 0$, the target slip model was not well reproduced (Figure 3c, data fit in Figure S3). With the application of the OTA, i.e., allowing T to vary in the range [0, 15] min, the offshore slip pattern was well recovered (Figure 3d, data fit in Figure S3).

When combining InSAR and tsunami data in a joint inversion without applying the OTA, the recovered slip model was poor (Figure 3e, InSAR data fit in Figure S4); we note that even the inland slip pattern was degraded with respect to the slip distribution recovered by inverting solely the InSAR data. Conversely, when using the OTA in the joint inversion, we obtained the best results both inland and offshore (Figure 3f). We also

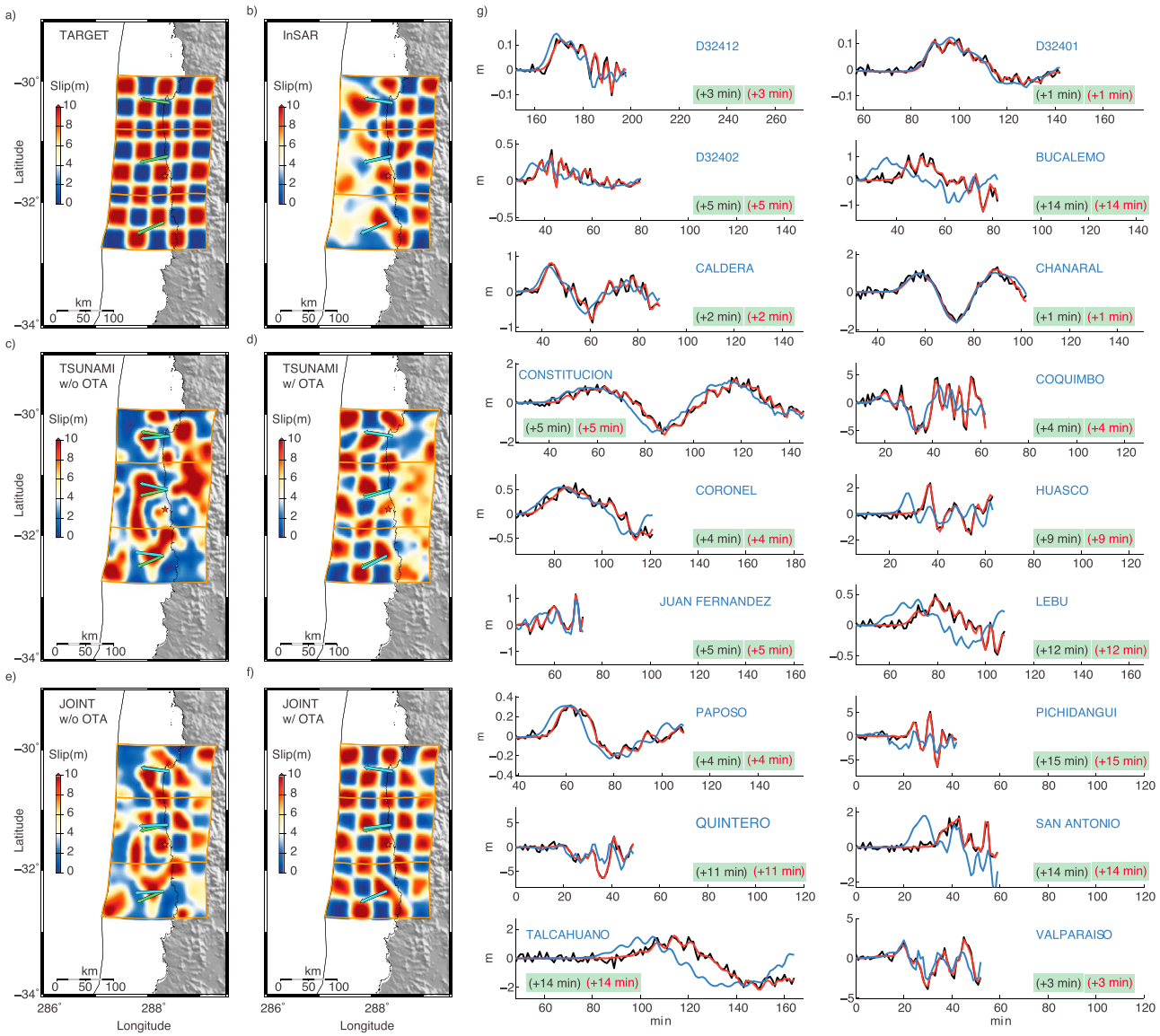

Figure 3. Synthetic tests. The panels show (a) target slip model, slip distribution retrieved (b) by inverting InSAR data, (c) by inverting tsunami data without OTA, (d) by inverting tsunami data applying OTA, (e) by jointly inverting tsunami and InSAR data without OTA, and (f) by jointly inverting tsunami and InSAR data applying OTA. The green and cyan arrows represent the target and predicted rake, respectively, inverted on large blocks (solid orange lines). (g) Comparison between target synthetic tsunami waveforms (black, slip model; Figure 3a) and predicted tsunami waveforms by jointly inverting tsunami and InSAR data with OTA (red) and without OTA (blue); the green labels indicate the waveform time shift assumed (black) and estimated applying the OTA method (red).

observed that the fit for both tsunami (Figure 3g) and InSAR (Figure S5) data was good and that the OTA is successfully applied to the tsunami waveforms. Finally, the assumed time shifts (see Figure 3g) are exactly recovered for all of the tsunami stations.

3. Application of the Method to a Real Case: The 2015 M_w 8.3 Illapel Earthquake

The Chilean margin is defined by the subduction of the Nazca plate under the South America plate with a relative convergence rate of 7.4 cm/yr [*De Mets et al.*, 2010]. This is one of the most seismically active zones in the world and has hosted a number of great earthquakes; for example, from 1535 to 1960 (the year of the *M*9.5 Valdivia earthquake, the largest seismic event ever recorded), ~20 $M >=8$ earthquakes occurred in the region, most of which were tsunamigenic [e.g., *Beck et al.*, 1998; *Lomnitz*, 2004]. In the recent past, two great megathrust tsunamigenic earthquakes occurred: the 2010 M_w 8.8 Maule [e.g., *Lorito et al.*, 2011] and the 2014 M_w 8.1 Iquique [e.g., *Gusman et al.*, 2015] events.

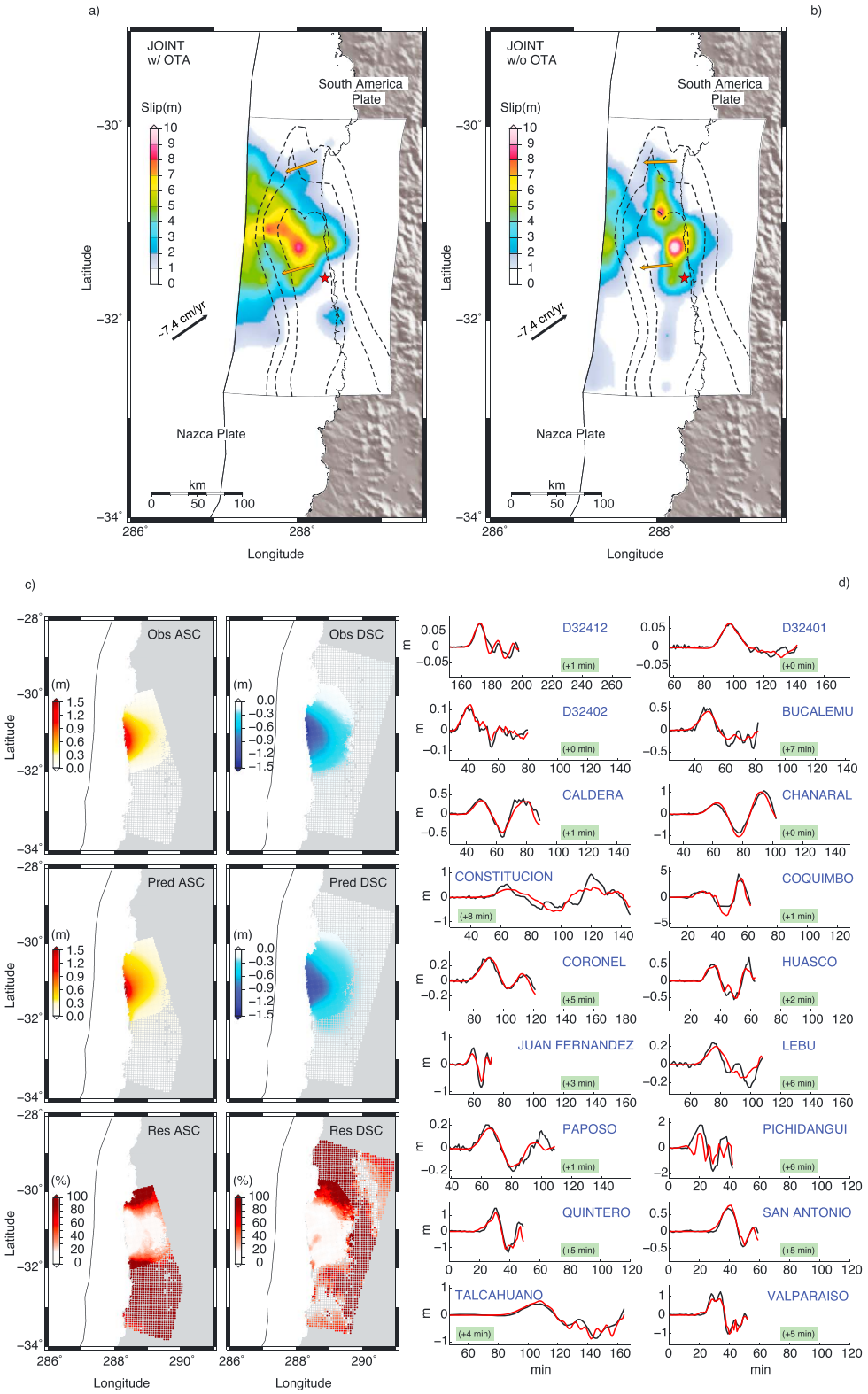

Figure 4. Source of the 16 September 2015 Illapel earthquake and data fit. Slip distribution obtained by jointly inverting tsunami and InSAR data (a) with OTA and (b) without OTA. The dashed black lines in Figures 4a and 4b indicate the interseismic coupling (contour 50, 70, and 90%) along the subduction interface in the area of the mainshock (red star). (c) Comparison between observed and predicted InSAR data and percentage residuals for (left column) ascending and (right column) descending orbit. (d) Comparison between observed (black) and predicted (red) tsunami data for model in Figure 4a. The green labels indicate the waveform time shift estimated applying the OTA method.

The hypocenter of the 16 September 2015 M_w 8.3 Illapel earthquake (71.67°W, 31.57°S, U.S. Geological Survey, http://earthquake.usgs.gov/earthquakes/eventpage/us20003k7a#executive) was located at a depth of ~23 km along the subduction interface between the Nazca and South America plates (Figure 2). This earthquake generated a tsunami that mainly struck the Chilean coasts from ~42°S to ~19°S with measured wave amplitudes from few decimeters to some meters (up to 4.7 m at the tide gauge in Coquimbo). The tsunami impact was significant (average observed runup >5 m [*Contreras-Lopez et al*., 2016; *Aránguiz et al*., 2016]) on a long stretch of the Chilean coast (>500 km), and in particular nearby Coquimbo (runup >10 m). Overall, the death toll has been very low, thanks to the evacuation of about one million people.

Significant tsunami waves resulting from the Illapel earthquake have been recorded by a number of tide gauges distributed along the entire Chilean coast, from ~37.5°S to ~25°S and by a tide gauge located along the coast of the Robinson Crusoe Island, in the Juan Fernández archipelago, southwestward from the epicenter. In addition, the tsunami propagated over the Pacific Ocean and was distinctly recorded by several DART buoys (http://www.ndbc.noaa.gov/dart.shtml). In this study, we used the tsunami waveforms from 15 tide gauges (managed by the Servicio Hidrográfico y Oceanográfico de la Armada, SHOA) and three DART buoys (32401, 32402, and 32412). Combining tide gauges with DARTs guarantees a good azimuthal coverage around the tsunami source (Table S2 and Figure 2). Tsunami waveforms (1 min sampling rate) were obtained by removing from each original signal the tidal contribution using a LOWESS procedure [*Barbosa et al*., 2004].

We adopted the standard Differential SAR Interferometry (InSAR) technique [*Franceschetti and Lanari*, 1999] to retrieve the static coseismic displacement field induced by the mainshock which occurred on 16 September 2015. We used SAR data acquired by the Sentinel1-A satellite between 26 August and 19 September, from the ascending orbit, and from 25 August to 17 September, from the descending orbit. Raw interferograms were filtered with the *Goldstein and Werner* [1998] algorithm and unwrapped with a Delaunay Minimum Cost Flow algorithm [*Costantini and Rosen*, 1999]. The two line-of-sight (LOS, the ground to satellite direction) displacement maps show similar patterns and intensities with opposite signs (positive ascending, negative descending, Figure 4c), as expected for this subduction zone earthquake where the signal has a predominant horizontal, westward, direction. The maximum displacement is ~1.5 m located along the coast, close to the city of Illapel.

We reduce the large amount of InSAR measurements, taking into account a double-sized regular mesh, and set the spatial resolution to 3 km in the epicentral area and 6 km far from it.

The tsunami and InSAR data were jointly inverted to investigate the coseismic rupture process of the Illapel earthquake. Assuming a circular rupture front with constant rupture velocity of 2 km/s [*Ye et al*., 2016a], we compared the slip distribution retrieved with and without the OTA method.

When the OTA method was applied to the tsunami waveforms we observe that the significant slip is mainly distributed NW from the hypocenter, with an elongated patch of slip with values greater than 7 m (maximum slip is 9 m) centered at ~287.7°E, ~31.2°S at a depth of ~15 km (Figure 4a), within an area characterized by a high locking degree (>90 % [*Métois et al*., 2012]). The overall coseismic rupture area roughly shows a triangular shape where one of the sides overlaps with the trench axis over a zone of ~190 km along strike from ~32°S to ~30.2°S; in particular, the rupture reaches the shallow part of the megathrust with an average slip of ~5 m from ~31.5°S to 30.5°S. The maximum rupture extents along dip, perpendicularly to the trench axis, for ~110 km (from ~287.4°E to ~288.5°E) with ~5 m of slip in the portion of the megathrust directly located under the continental part of the South America plate. On the other hand, when the "classical" approach (i.e., without OTA) was applied, the pattern of slip is significantly different, with the main patch of slip (Figure 4b, data fit in Figures S6 and S7) shifted landward and fairly well separated from a second shallow patch featuring lower slip values with respect to the previous model. This illustrates the expected trade-off between the slip placement and the arrival times at the tide gauges. Together with the results from the synthetic tests, this indicates that without applying the OTA to tide-gauge data the resulting slip model might feature misplaced slip patches. Moreover, the cost function value for tsunami waveforms (equation (1)) is lower (0.16) when we apply the OTA method (0.33 without OTA).

The slip model retrieved by using OTA predicts the tsunami waves observed both at the DARTs and at the tide gauge well (Figure 4d); the average estimated time mismatch between modeled and observed tsunami waveforms at the tide gauges is ~4 min, which is consistent with the uncertainty in the local bathymetry and tide-gauge position [*Heidarzadeh and Satake*, 2014].

It is interesting to notice that the estimated time shift for the DART buoys is null for the sensors 32402 and 32401, whereas the time shift is equal to 1 min for the sensor 32412. Mild time shifts are also possible at DARTs for a number of different reasons: neglected ocean floor elasticity, depth variation of the water density, dispersion, and geopotential gravity changes associated to tsunami propagation [e.g., *Tsai et al*., 2013; *Watada et al*., 2014]. However, they seem very limited in the present case, which is mostly likely due to the relatively short source-sensor distance. This confirms that these data are more easily modeled than tide gauges when using a relatively coarse bathymetry model and that the time delay observed at the tide gauges is accumulated during tsunami propagation near the coastline or due to the instrumental response.

The comparison between observed and predicted InSAR deformation is satisfactory for both the ascending and descending orbits with the percentage residuals lower than 20% in the area of large deformation (absolute value $>$40 cm; Figure 4c); the highest residuals appear in the areas where the coseismic deformation is relatively negligible.

Our preferred slip model (Figure 4a) is in a first-order agreement with previously published models of the same event [e.g., *Melgar et al*., 2016; *Tilmann et al*., 2016; *Ye et al*., 2016b; *Lay et al*., 2016; *Lee et al*., 2016]: in fact, all of these models show a V-shaped slip distribution mainly extending NW from the epicenter and similar to that shown in Figure 4a.

Second-order differences with other models regard the details of the slip pattern and the maximum slip values. For example, the model by *Lee et al.* [2016] which inverted teleseismic data contains a secondary and significant shallow patch of slip south of ~32°S, which is not present in our preferred slip model nor in the model by *Lay et al.* [2016]; however, we did not analyze the possible trade-off caused by delayed slip with rupture position and the retrieved time shifts. The source model by *Melgar et al.* [2016] could be viewed as an intermediate model between our preferred model obtained by applying OTA (Figure 4a) and the slip distribution we retrieved when the OTA is not applied (Figure 4b). Indeed, whereas the latter shares the deeper patch of slip shown in *Melgar et al.* [2016] that is centred around ~31°S, the slip distribution obtained with the OTA shares the shallower rupture extent but with relatively lower slip values compared to *Melgar et al.* [2016]. We also observe that the time mismatches between some observed and predicted tsunami waveforms used in *Melgar et al.* [2016] are comparable with the ones found in the present study (e.g., at Bucalemu and Constitucion); however, we do not know how these time mismatches are eventually mapped in the *Melgar et al.*'s [2016] slip model, since they inverted a set of data very different from ours.

Our preferred slip model also features an average rake of ~112° north of the epicenter that is consistent with the relative convergence direction between the Nazca and South America plates. The seismic moment estimated from the slip distribution of the Illapel earthquake is $M_0 = 2.82 \times 10^{21}$ Nm, corresponding to a moment magnitude $M_w = 8.3$ (rigidity = 30 GPa). Based on the slip distribution in Figure 4a, the average stress drop weighted by the slip [*Noda et al*., 2013] is 4.9 MPa. This is consistent with the average slip-weighted stress drop (3.4–4.6 MPa) observed by *Ye et al.* [2016b] across a catalogue of +*M*7 events and is slightly higher than the values (2.6–4.0 MPa) obtained by *Ye et al.* [2016a] for the Illapel earthquake.

4. Conclusion

We propose a method that allows the automatic estimation and correction of possible time mismatch between observed and predicted tide-gauge tsunami waveforms when inverting for the tsunami source. This method, here termed optimal time alignment (OTA), avoids mapping of time shifts onto source features, while also retrieving the actual time shifts self-consistently along with the source parameters during a nonlinear inversion.

We analyzed the effectiveness of the method by means of a series of synthetic tests in which tsunami waveforms have been randomly shifted in time further than being as usual corrupted with noise. Our findings indicate that if the time shift between observed and modeled tsunami waveform is overlooked then the target slip model cannot be properly recovered; in other words, the resolution on the slip model seriously degrades, which may not appear if a synthetic test does not consider time shifts. The OTA method does not account for inverting for the temporal features of the ruptures, which if particularly prominent, may be mapped into the retrieved time shifts which in turn would result in the misplacement of some slip patches.

We also applied the OTA method to retrieve the tsunami source of a real event, namely, the 16 September 2015, M_w 8.3, Illapel earthquake by jointly inverting tsunami and InSAR data (in order to exploit the complementary resolving power of the two data sets). We found that the coseismic slip was predominantly distributed to the NW of the hypocenter, with a maximum of ~9 m at ~15 km depth and significantly large slip (i.e., up to 5 m) in the shallow part of the megathrust. In particular, the average estimated time mismatch between predicted and observed tide-gauge tsunami waveforms was ~4 min. Without the application of the OTA method, the inversion would produce a significantly different model, with most of the slip shifted toward the Chilean coast.

Acknowledgments
We thank the UNESCO Intergovernmental Oceanographic Commission for providing tsunami data (http://www.ioc-sealevelmonitoring.org/) and the European Space Agency for providing the Sentinel1-A data (http://scihub.copernicus.eu/dhus/#/home). Figures were made by using GMT and MATLAB. This work has been partially funded by EC project ASTARTE—Assessment, STrategy And Risk Reduction for Tsunamis in Europe, grant 603839, 7th FP (ENV.2013.6.4-3 ENV.2013.6.4-3), and the Italian Flagship Project RITMARE.

References

Aránguiz, R., et al. (2016), The 16 September 2015 Chile tsunami from the post-tsunami survey and numerical modeling perspectives, *Pure Appl. Geophys.*, *173*, 333–348, doi:10.1007/s00024-015-1225-4.

Barbosa, S. M., M. J. Fernandes, and M. E. Silva (2004), Nonlinear sea level trends from European tide gauge records, *Ann. Geophys.*, *22*, 1465–1472, doi:10.5194/angeo-22-1465-2004.

Beck, S., S. Barrientos, E. Kausel, and M. Reyes (1998), Source characteristics of historic earthquakes along the central Chile subduction zone, *J. South Am. Earth Sci.*, *11*, 115–129.

Bletery, Q., A. Sladen, B. Delouis, M. Vallée, J. M. Nocquet, L. Rolland, and J. Jiang (2014), A detailed source model for the M_w9.0 Tohoku-Oki earthquake reconciling geodesy, seismology, and tsunami records, *J. Geophys. Res. Solid Earth*, *119*, 7636–7653, doi:10.1002/2014JB011261.

Contreras-Lopez, M., et al. (2016), Field survey of the 2015 Chile tsunami with emphasis on coastal wetland and conservation areas, *Pure Appl. Geophys.*, *173*, doi:10.1007/s00024-015-1235-2.

Costantini, M., and P. A. Rosen (1999), A generalized phase unwrapping approach for sparse data, *IGARSS '99 Proc. IEEE 1999 Int.*, *1*, 267–269, doi:10.1109/IGARSS.1999.773467.

DeMets, C., R. G. Gordon, and D. F. Argus (2010), Geologically current plate motions, *Geophys. J. Int.*, *181*, 1–80, doi:10.1111/j.1365-246X.2009.04491.x.

Franceschetti, G., and R. Lanari (1999), *Synthetic Aperture Radar Processing*, 328 pp., CRC Press, Boca Raton, Fla.

Fujii, Y., and K. Satake (2006), Source of the July 2006 West Java tsunami estimated from tide gauge records, *Geophys. Res. Lett.*, *33*, L24317, doi:10.1029/2006GL028049.

Goldstein, R. M., and C. Werner (1998), Radar interferogram filtering for geophysical applications, *Geophys. Res. Lett.*, *25*, 4035–4038, doi:10.1029/1998GL900033.

Gusman, A. R., S. Murotani, K. Satake, M. Heidarzadeh, E. Gunawan, S. Watada, and B. Schurr (2015), Fault slip distribution of the 2014 Iquique, Chile, earthquake estimated from ocean-wide tsunami waveforms and GPS data, *Geophys. Res. Lett.*, *42*, 1053–1060, doi:10.1002/2014GL062604.

Hayes, G. P., D. J. Wald, and R. L. Johnson (2012), Slab1.0: A three-dimensional model of global subduction zone geometries, *J. Geophys. Res.*, *117*, B01302, doi:10.1029/2011JB008524.

Heidarzadeh, M., and K. Satake (2014), Possible sources of the tsunami observed in the northwestern Indian Ocean following the 2013 September 24 Mw 7.7 Pakistan inland earthquake, *Geophys. J. Int.*, *199*(2), 752–766, doi:10.1093/gji/ggu297.

Heidarzadeh, M., S. Murotani, K. Satake, T. Ishibe, and A. R. Gusman (2016), Source model of the 16 September 2015 Illapel, Chile, Mw 8.4 earthquake based on teleseismic and tsunami data, *Geophys. Res. Lett.*, *43*, 643–650, doi:10.1002/2015GL067297.

Kajiura, K. (1963), The leading wave of a tsunami, *Bull. Earthq. Res. Inst. Univ. Tokyo*, *41*, 535–571.

Kimman, W. P. (2016), Surface consistent finite frequency phase corrections, *Geophys. J. Int.*, *206*(1), 420–437, doi:10.1093/gji/ggw143.

Lay, T. (2015), The surge of great earthquakes from 2004 to 2014, *Earth Planet. Sci. Lett.*, *409*, 133–146, doi:10.1016/j.epsl.2014.10.047.

Lay, T., L. Li, and K. F. Cheung (2016), Modeling tsunami observations to evaluate a proposed late tsunami earthquake stage for the 16 September 2015 Illapel, Chile, MW 8.3 earthquake, *Geophys. Res. Lett.*, *43*, 7902–7912, doi:10.1002/2016GL070002.

Lee, S.-J., T. Y. Yeh, T. C. Lin, Y. Y. Lin, T. R. A. Song, and B. S. Huang (2016), Two-stage composite megathrust rupture of the 2015 Mw8.4 Illapel, Chile, earthquake identified by spectral-element inversion of teleseismic waves, *Geophys. Res. Lett.*, *43*, 4979–4985, doi:10.1002/2016GL068843.

Lomnitz, C. (2004), Major earthquakes of Chile: A historical survey, 1535–1960, *Seismol. Res. Lett.*, *75*(3), 368–378.

Lorito, S., F. Romano, S. Atzori, X. Tong, A. Avallone, J. McCloskey, M. Cocco, E. Boschi, and A. Piatanesi (2011), Limited overlap between the seismic gap and coseismic slip of the great 2010 Chile earthquake, *Nat. Geosci.*, *4*, 1073, doi:10.1038/NGEO1073.

Lorito, S., F. Romano, and T. Lay (2016), Tsunamigenic earthquakes (2004–2013): Source processes from data inversion, Solicited Paper, in *Encyclopedia of Complexity and Systems Science*, edited by R.A. Meyers, Springer Science + Business Media, New York, doi:10.1007/978-3-642-27737-5_641-1.

Meade, B. J. (2007), Algorithms for the calculation of exact displacements, strains, and stresses for triangular dislocation elements in a uniform elastic half space, *Comput. Geosci.*, *33*, 1064–1075, doi:10.1016/j.cageo.2006.12.003.

Melgar, D., W. Fan, S. Riquelme, J. Geng, C. Liang, M. Fuentes, G. Vargas, R. M. Allen, P. M. Shearer, and E. J. Fielding (2016), Slip segmentation and slow rupture to the trench during the 2015, Mw8.3 Illapel, Chile earthquake, *Geophys. Res. Lett.*, *43*, 961–966, doi:10.1002/2015GL067369.

Mercerat, E. D., and G. Nolet (2013), On the linearity of cross-correlation delay times in finite-frequency tomography, *Geophys. J. Int.*, *192*(2), 681–697, doi:10.1093/gji/ggs017.

Métois, M., A. Socquet, and C. Vigny (2012), Interseismic coupling, segmentation and mechanical behavior of the central Chile subduction zone, *J. Geophys. Res.*, *117*, B03406, doi:10.1029/2011JB008736.

Noda, H., N. Lapusta, and H. Kanamori (2013), Comparison of average stress drop measures for ruptures with heterogeneous stress change and implications for earthquake physics, *Geophys. J. Int.*, *193*, 1691–1712, doi:10.1093/gji/ggt074.

Piatanesi, A., and S. Lorito (2007), Rupture process of the 2004 Sumatra-Andaman earthquake from tsunami waveform inversion, *Bull. Seismol. Soc. Am.*, *97*(1A), S223–S231, doi:10.1785/0120050627.

Romano, F., A. Piatanesi, S. Lorito, and K. Hirata (2010), Slip distribution of the 2003 Tokachi-oki Mw 8.1 earthquake from joint inversion of tsunami waveforms and geodetic data, *J. Geophys. Res.*, *115*, B11313, doi:10.1029/2009JB006665.

Romano, F., A. Piatanesi, S. Lorito, N. D'Agostino, K. Hirata, S. Atzori, Y. Yamazaki, and M. Cocco (2012), Clues from joint inversion of tsunami and geodetic data of the 2011 Tohoku-oki earthquake, *Sci. Rep.*, *2*, 385, doi:10.1038/srep00385.

Romano, F., E. Trasatti, S. Lorito, C. Piromallo, A. Piatanesi, Y. Ito, D. Zhao, K. Hirata, P. Lanucara, and M. Cocco (2014), Structural control on the Tohoku earthquake rupture process investigated by 3D FEM, tsunami and geodetic data, *Sci. Rep.*, *4*, 5631, doi:10.1038/srep05631.

Romano, F., I. Molinari, S. Lorito, and A. Piatanesi (2015), Source of the 6 February 2013 Mw = 8.0 Santa Cruz Islands Tsunami, *Nat. Hazards Earth Syst. Sci.*, *15*, 1371–1379, doi:10.5194/nhess-15-1371-2015.

Rothman, D. (1986), Automatic estimation of large residual statics corrections, *Geophysics*, *51*, 332–346, doi:10.1190/1.1442092.

Satake, K. (1987), Inversion of tsunami waveforms for the estimation of a fault heterogeneity: Method and numerical experiment, *J. Phys. Earth*, *35*, 241–254.

Satake, K., Y. Fujii, T. Harada, and Y. Namegaya (2013), Time and space distribution of coseismic slip of the 2011 Tohoku earthquake as inferred from tsunami waveform data, *Bull. Seismol. Soc. Am.*, *103*, 1473–1492, doi:10.1785/0120120122.

Simons, M., et al. (2011), The 2011 magnitude 9.0 Tohoku-Oki earthquake: Mosaicking the megathrust from seconds to centuries, *Science*, *332*, 1421–1425, doi:10.1126/science.1206731.

Tanioka, Y., and K. Satake (1996), Tsunami generation by horizontal displacement of ocean bottom, *Geophys. Res. Lett.*, *23*, 861–864, doi:10.1029/96GL00736.

Tilmann, F., et al. (2016), The 2015 Illapel earthquake, central Chile: A type case for a characteristic earthquake? *Geophys. Res. Lett.*, *43*, 574–583, doi:10.1002/2015GL066963.

Tsai, V. C., J. P. Ampuero, H. Kanamori, and D. J. Stevenson (2013), Estimating the effect of Earth elasticity and variable water density on tsunami speeds, *Geophys. Res. Lett.*, *40*, 492–496, doi:10.1002/grl.50147.

Van Decar, J. C., and R. S. Crosson (1990), Determination of teleseismic relative phase arrival times using multi-channel cross-correlation and least squares, *Bull. Seismol. Soc. Am.*, *80*(1), 150–169.

Watada, S., S. Kusumoto, and K. Satake (2014), Traveltime delay and initial phase reversal of distant tsunamis coupled with the self-gravitating elastic Earth, *J. Geophys. Res. Solid Earth*, *119*, 4287–4310, doi:10.1002/2013JB010841.

Yamazaki, Y., Z. Kowalik, and K. F. Cheung (2009), Depth-integrated, non-hydrostatic model for wave breaking, *Int. J. Numer. Meth. Fluids*, *61*, 473–497, doi:10.1002/fld.1952.

Yamazaki, Y., K. F. Cheung, and Z. Kowalik (2011), Depth-integrated, non-hydrostatic model with grid nesting for tsunami generation, propagation, and run-up, *Int. J. Numer. Meth. Fluids*, *67*, 2081–2107, doi:10.1002/fld.2485.

Ye, L., T. Lay, H. Kanamori, and K. D. Koper (2016a), Rapidly estimated seismic source parameters for the 16 September 2015 Illapel, Chile Mw 8.3 earthquake, *Pure Appl. Geophys.*, *173*, 321–332, doi:10.1007/s00024-015-1202-y.

Ye, L., T. Lay, H. Kanamori, and L. Rivera (2016b), Rupture characteristics of major and great (Mw $\geq$ 7.0) megathrust earthquakes from 1990 to 2015: 1. Source parameter scaling relationships, *J. Geophys. Res. Solid Earth*, *121*, 826–844, doi:10.1002/2015JB012426.

Yuan, Y. O., F. J. Simons, and J. Tromp (2016), Double-different adjoint seismic tomography, *Geophys. J. Int.*, *206*(3), 1599–1618, doi:10.1093/gji/ggw233.

Zhang, H., and C. H. Thurber (2003), Double-difference tomography: The method and its application to the Hayward fault, California, *Bull. Seismol. Soc. Am.*, *93*(5), 1875–1889, doi:10.1785/0120020190.